Journal of Power Sources 198 (2012) 7–13

Contents lists available at SciVerse ScienceDirect

Journal of Power Sources

journal homepage: www.elsevier.com/locate/jpowsour

Phosphine impurity tolerance of $Sr_2MgMoO_{6-\delta}$ composite SOFC anodes

Phil Gansor[a,*], Chunchuan Xu[b], Katarzyna Sabolsky[a], John W. Zondlo[b], Edward M. Sabolsky[a]

[a] Department of Mechanical and Aerospace Engineering, West Virginia University, Morgantown, WV 26506, United States
[b] Department of Chemical Engineering, West Virginia University, Morgantown, WV 26506, United States

ARTICLE INFO

Article history:
Received 19 August 2011
Received in revised form
20 September 2011
Accepted 21 September 2011
Available online 4 October 2011

Keywords:
SOFC
Anode
$Sr_2MgMoO_{6-\delta}$
Double-Perovskite
Phosphine

ABSTRACT

An all-ceramic solid-oxide fuel cell (SOFC) anode composed of a mixture of $Sr_2MgMoO_{6-\delta}$ (SMM) and $Ce_{0.9}Gd_{0.1}O_2$ (GDC) on a yttrium-stabilized zirconia (YSZ) electrolyte was synthesized and tested in clean and phosphine-contaminated hydrogen and coal syngas. The initial electrochemical performance of the cell at 800 °C was 290 mW cm^{-2} and 180 mW cm^{-2} in wet H_2 and in clean syngas, respectively. The same cell was tested in wet H_2 with 10 ppm PH_3, where the cell displayed stable performance over the first 40 h, but then slowly degraded over the next 80 h leading to a 47% decrease in power output (0.59 h^{-1} %). Although the anode showed notable degradation over the 120 h test, the performance was much improved compared to typical Ni/YSZ cermet anodes. XPS results did not detect P at the anode/electrolyte interface nor throughout the bulk of the anode in either a phosphide or phosphate form. While still unclear, this initial work suggests that degradation of the cell may be due to partial de-lamination of the cell at the anode/electrolyte interface.

1. Introduction

Solid Oxide Fuel Cells (SOFCs) have garnered a great deal of attention in recent years as a potential source of emission-free energy for both small mobile auxiliary power as well as for megawatt scale stationary power [1,2]. Most commercialized SOFCs operate on hydrogen fuel; however, operating SOFCs with fossil fuels is highly desirable due to their low cost and availability. For example, the use of coal syngas produced through various efficient gasification processes could push energy generation efficiency upwards of 60% [3]. The most commonly used SOFC anode, a nickel/yttrium-stabilized zirconia (Ni/YSZ) cermet, exhibits an ability to run in various clean syngas compositions [4–6], which has resulted in countless research efforts attempting to demonstrate actual functionality and stability in "dirty" gasified coal. Gasified coal contains H_2, CO, and residual CH_4 which serve as the primary fuel for the SOFC. The major limitation is that this same fuel stream is loaded with contaminants such as S, P, Sb, Cl, Zn, As, and HCl that react with the Ni-based anodes and quickly degrade the performance of the SOFC at standard operating temperatures. The reaction of nickel with these impurities can ultimately lead to resistive secondary phase formation, which results in a decrease in active sites and also a decrease in mass transport as these phases form within the porous anode structure.

Among the most reactive with nickel is phosphorus. Krishnan [7] and Trembly et al. [8] reported that their loss in cell performance is brought on from zirconia phosphate formation at the anode/electrolyte active interface. Both papers suggest that this results in a loss of the overall electrolyte ionic conductivity. Zhi et al. [9] report total cell degradation within 20 h of introducing 20 ppm PH_3 into the anode stream of an anode-supported cell. They attributed this failure to phosphorus reactions with both Zr and Ni. Marina et al. [10] conducted similar work, but expanded it to show clear boundaries between reacted and un-reacted Ni particles and also determined that Ni–P formation can occur at impurity concentrations less than 1 ppb. This is valuable information since current cleanup technologies display difficulties in removing phosphorus to this level in an economic manner.

Sulfur has also shown to be harmful to cell performance, though the failure mechanism is different than that of phosphorus. The sulfur affects the Ni/YSZ anode first through a surface adsorption process that occurs within a matter of seconds which raises the overall work function of nickel [11–13]. That process has been shown to be somewhat reversible upon removal of sulfur from the anode stream. However, solid Ni–S phase formation is also found during long-term operation in fuels containing sulfur, and this process has been proven to be irreversible [14,15].

Some progress has been made in regards to the prevention of sulfur poisoning of the nickel-based anode with the introduction of doped ceria into the anode either in conjunction with or in place of YSZ. In fact, a Ni/GDC (gadolinium doped ceria) anode was observed to withstand up to 200 ppm H_2S in syngas with

* Corresponding author. Tel.: +1 304 216 1330; fax: +1 304 293 6689.
E-mail address: pgansor@mix.wvu.edu (P. Gansor).

0378-7753/$ – see front matter © 2011 Elsevier B.V. All rights reserved.
doi:10.1016/j.jpowsour.2011.09.069

10–12% cell degradation after about 570 h of operation, which is an improvement over the Ni/YSZ anode but not a proven solution [16]. The GDC has been shown to be a good H_2S absorbent for SOFC [17], and GDC appears to react with sulfur to form ceria-sulfides at concentrations higher than 450 ppm from thermodynamic calculations [18–21]. This means that a Ni/GDC anode may be suitable for gasified coal as current technologies containing sulfur scrubbers display concentrations much lower than 450 ppm.

Another way to address the anode contaminant issue is to remove nickel from the anode entirely. Many different anodes have been developed previously for the investigation of fuel flexibility and impurity tolerance. A popular all-ceramic anode that has demonstrated stability in fuels containing low levels of H_2S is $SrTiO_3$. Pillai et al. [22] reported on an anode-supported $SrTiO_3$ anode capable of withstanding up to 100 ppm H_2S without appreciable degradation. Kurokawa et al. [23] demonstrated stable cell performance in upwards of 40 ppm H_2S with A-site doping with Y and Ce and Ru infiltration. $La_{0.75}Sr_{0.25}Cr_{1-x}Mn_xO_3$ is another anode that has been shown by Zha et al. [24] to resist sulfur poisoning, however the level of H_2S tolerance is strongly dependent upon the amount of Cr in the anode matrix. A WS_2 anode, developed by Yates and Winnick [25] has shown short term tolerance (~24 h) to direct H_2S fuel. Cheng et al. have recently developed a strontium-doped lanthanum vanadate anode ($La_{1-x}Sr_xVO_3$) that exhibits sulfur tolerance and favorability to a sulfur-containing environment for upwards of 48 h. However, the perovskite structure of this anode tends to lose its integrity over longer operation times and secondary phases form which inhibit the cells ability to perform [26].

Several double perovskite structured anode materials ($A_2BB'O_6$) have been investigated with $Sr_2MgMoO_{6-\delta}$ being among the best in terms of resistance to sulfur poisoning. Goodenough and Huang [27] and Huang et al. [28,29] have applied this anode to a $La_{0.8}Sr_{0.2}Ga_{0.83}Mg_{0.17}O_{2.815}$ (LSGM) electrolyte with the use of a lanthanum-doped ceria (LDC) interlayer to prevent interfacial reactions between the electrodes and electrolytes. They have achieved power densities of 500 mW cm^{-2} in CH_4 and 840 mW cm^{-2} in H_2 at 800 °C using $SrCo_{0.8}Fe_{0.2}O_{3-\delta}$ (SCF) as a cathode. This anode also is capable of operating in up to 50 ppm H_2S in H_2 with minimal performance loss after 200 h (~5% voltage loss).

Since the SMM anode has been shown to perform well in a variety of fuels and withstand realistic levels of H_2S, a logical progression would be to investigate how this anode responds to other coal contaminants. Specifically, this study will investigate the response of the cell upon introducing 10 ppm PH_3 into the H_2 anode stream. One issue with this anode is that the SMM alone exhibits relatively low ionic conductivity in reducing atmospheres [30]; thus, GDC is incorporated into the anode to improve the ionic conduction of the cell.

2. Experimental

2.1. $Sr_2MgMoO_{6-\delta}$ powder preparation

$Sr_2MgMoO_{6-\delta}$ powders were synthesized using a standard solid-state method with $SrCO_3$, MgO, and MoO_3 (Alfa Aesar, 99.9% purity for each) as starting reagent materials. The powders were first mixed and then ball milled in ethanol and calcined at 1000 °C for 4 h in air to burn off the carbonates. After the initial heat treatment, the powder was sieved and attrition-milled for 4 h. The powder was then calcined at the same temperature and time under a reducing atmosphere (5% H_2/N_2) to form the single-phase SMM material. Previous work on this material suggests that the low melting temperature and high volatility of Mo make it problematic for high thermal treatment temperatures [30], so the lowest possible calcination temperature was sought to minimize this effect.

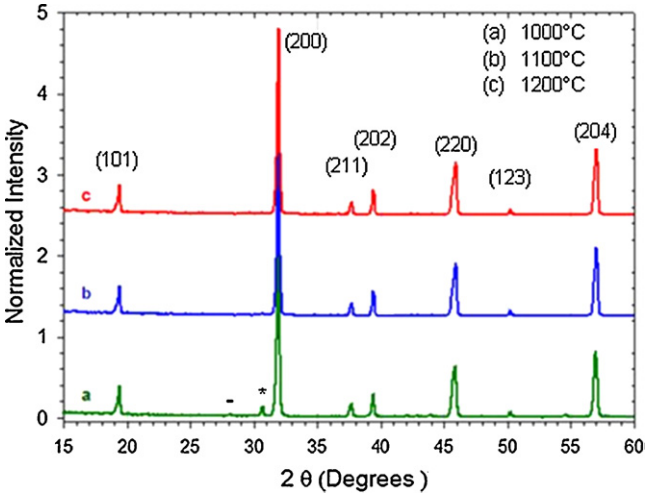

Fig. 1. XRD spectra for the $Sr_2MgMoO_{6-\delta}$ anode calcined at different temperatures in a 5% H_2/N_2 atmosphere. (-) and (*) represent the secondary phases $SrMoO_4$ and Sr_3MoO_6 respectively.

X-ray diffraction (XRD) spectra were recorded for samples fired at 1000 °C, 1100 °C, and 1200 °C for 4 h in 5% H_2/N_2 and are shown in Fig. 1. At 1000 °C and 1100 °C, a secondary scheelite phase ($SrMoO_4$) was detected at 27.5° (2θ). A single phase material was formed at 1200 °C and the bulk of the powder was calcined at this temperature. Recent work by Vasala et al. [31] suggests that the $SrMoO_4$ phase is an insulator, but that it becomes $SrMoO_3$ in atmospheres with low partial pressures of oxygen and the reduced structure is conductive. Thus, at 1200 °C, a nearly single phase was achieved, and the traces of $SrMoO_4$ present (<1%) were deemed insignificant with regard to electrode performance. The final step in powder synthesis was attrition milling to achieve unimodal particle size distribution. The BET surface area of this calcined powder was found to be 4.711 m^2 g^{-1}, which is greater than SMM powders prepared elsewhere [32].

2.2. Electrolyte/GDC preparation and processing

Most of the previous fuel cell experiments carried out with the SMM anode utilized LSGM as the electrolyte due to its higher ionic conductivity [27]. However, the material is quite brittle and still highly reactive; thus, 8 mol% Y_2O_3–ZrO_2 (YSZ) electrolyte substrates were used for our anode evaluations. YSZ powder (Daiichi Kigenso Kagaku Kogoyo Co., Ltd.) was first mixed into a slurry using the appropriate amounts of a 50/50 wt% xylene/ethanol solvent system and a fish-oil dispersant. After milling for 4 h the plasticizers (benzyl butyl phthalate and poly-alkalene glycol) and poly-vinyl butyral binder were added to the system and milled for 12 h.

The slurry was then tape casted onto mylar sheets to a dried thickness of approximately 50 μm. Pieces of this tape were cut and layered so that a green thickness of 150 μm was achieved. The stacked YSZ sheets were laminated at 100 °C and 0.4 GPa. Laminates were cut into 1 cm diameter button cells generated by sintering at 1450 °C for 2 h. The final thickness of the YSZ electrolytes was approximately 120 μm, which provides a structurally sound support and allows for qualitative and quantitative anode performance comparisons. The GDC used in this study was prepared using a conventional co-precipitation method [33].

2.3. Button cell assembly

Button cells were produced by first taking the YSZ electrolytes and applying a GDC buffer layer onto both sides and sintering at

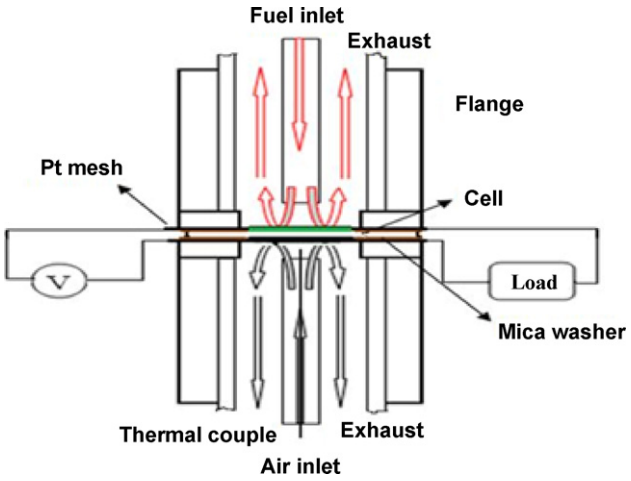

Fig. 2. Fuel cell fixture schematic used in current–voltage–power (*J–V–P*) testing in this work.

1400 °C for 2 h for optimal density. The first set of cells contained an anode approximately 40 μm in thickness of SMM and was fired on at 1100 °C for 2 h. The second set of cells had a different anode composition, where the anode was composed of a 40 μm composite anode (50 wt% SMM and 50 wt% GDC). The composite anode was applied to one side and fired at 1150 °C for 2 h. For both sets, a $La_{0.85}Sr_{0.15}MnO_3$ (LSM) based cathode was used. The cathode consists of a 10 μm LSM/GDC active cathode layer which was printed and then dried before adding a 40 μm LSM current collector layer. This cathode assembly was sintered at 1100 °C for 1 h.

2.4. Fuel cell testing

Prior to testing, a pair of 6 mm × 50 mm platinum mesh (80 mesh woven) strips were attached with platinum paste to serve as the current collector. The cells were then mounted between two alumina flanges with mica washers for a compressed seal configuration shown in Fig. 2. Each end of Pt mesh at both electrodes was connected to a thick sliver wire for the current lead and a thin wire for the voltage lead. The cell was heated to 800 °C at a rate 2 °C min^{-1} in 50 sccm N_2 on the anode and air on the cathode. After the target 800 °C was reached, the fuel stream was slowly converted to the wet H_2 fuel. A 0.25 A cm^{-2} constant current was loaded on the cell with 100 sccm wet H_2 (97% H_2, and 3% H_2O) to the anode and 150 sccm air flow to the cathode. After the cell voltage stabilized for 20 h, the cell polarization curve (*J–V* curve) and electrochemical impedance spectrum (EIS) were taken to establish the cell baseline performance. The EIS were collected using a Solartron SI-1287 electrochemical interface and an SI-1252 frequency response analyzer. An AC amplitude of 20 mV at frequencies ranging from 200 kHz to 0.1 Hz was applied for the EIS testing. The constant DC current load was supplied by a solid-state load cell (TDI Transistor Device SD-1103). PH_3 was added in the fuel downstream before the furnace. The fuel transport tubes were per-heated to over 150 °C. After testing, the cell was cooled to room temperature by purging 30% H_2 and 70% N_2 to the anode.

3. Results and discussion

3.1. Initial performance of the SMM anode in clean H_2 fuel

The goal of the initial tests was to establish a baseline performance for the pure SMM anode in order to later assess the effects of the phosphine additions on the degradation of the anode. Table 1 shows the cell performance for various anode sintering temperatures and indicates that the performance of the cell increases as the sintering temperature decreases. This would suggest that the higher sintering temperature may alter the porosity level and triple-phase boundary area, and/or may result in potential interfacial reactions between the anode and electrolyte, even with a dense GDC interlayer. Sintering studies at temperatures below 1100 °C were investigated, but these temperatures were not found to be high enough for proper adherence of the anode to the electrolyte. The cells were found to be stable over the course of 48 h, but the maximum power density achieved was only 110 mW cm^{-2} for the cell with the anode fired at 1100 °C.

Table 1
Max power densities for both SMM and GDC anode.

Sample	Sintering temp. (°C)	SMM (mW cm^{-2})	GDC (mW cm^{-2})
1	1350	65	–
2	1300	70	–
3	1250	85	–
4	1200	100	–
5	1150	100	–
6	1100	110	60

3.2. Performance of SMM/GDC anode in clean H_2 fuel and clean coal syngas blend

In an effort to enhance the performance of the cell, the GDC was added to the anode matrix to form a 50/50 wt% mixture with SMM. The addition of the GDC within the anode to the baseline cell resulted in a cell performance of ~280 mW cm^{-2} in wet H_2. This cell also remained stable for over 4 days without significant degradation (~0.008 h^{-1} %, time not shown). Previous investigations suggest that structural changes to the ceria in the reducing atmospheres can decrease cell performance over time. The testing conducted in this study showed essentially no loss in performance when operating on pure H_2 with the SMM/GDC composite anode. This was important to establish so that the possibility of the cell deteriorating in the presence of H_2 alone might be eliminated. For an electrolyte-supported cell, this performance and stability was found suitable for the contaminant investigation. Fig. 3 shows the *J–V* performance curve for the baseline SMM/GDC cell in wet H_2.

To establish the SMM/GDC anode as suitable for long term power generation in a coal syngas-based fuel stream, the anode must demonstrate reasonable performance in wet syngas with trace levels of impurities. To test the viability of this anode in a coal-based fuel environment, a cell was loaded and stabilized in wet H_2. After power stabilization, the cell was exposed to a fuel environment with 34% H_2, 31% CO, 19% CO_2, and 16% H_2O, which simulates a standard coal syngas composition. In Fig. 4 the expected decrease in the cell potential can be seen as a result of the syngas fuel composition. The maximum power density of this cell in syngas was

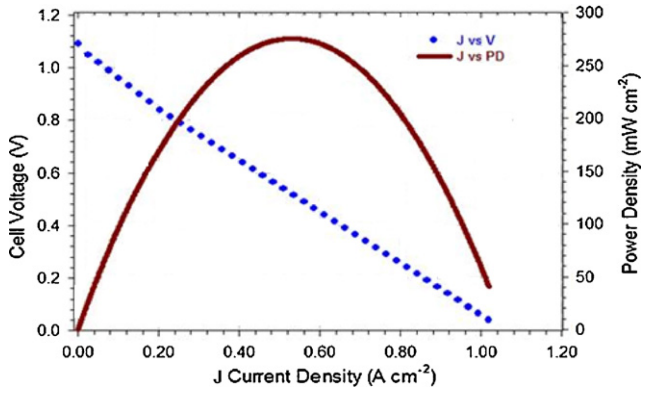

Fig. 3. (*J–V–P*) performance for SMM/GDC composite anode in wet H_2 (3% H_2O).

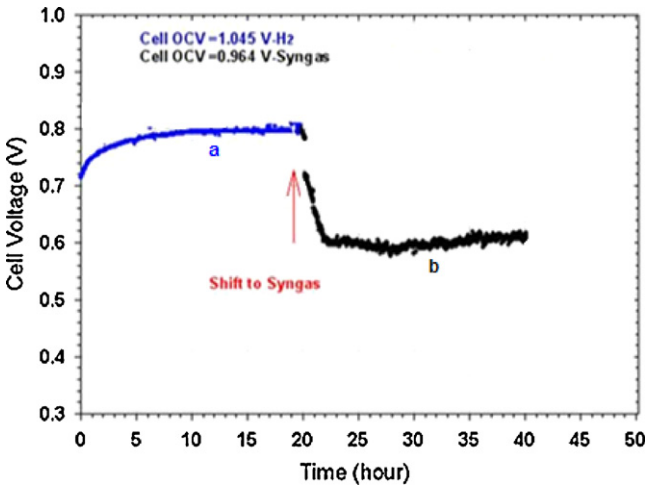

Fig. 4. Voltage vs. time for the electrolyte-supported SOFC with a SMM/GDC anode tested at constant current density (0.25 A cm^{-2}) in (a) H_2 + 3% H_2O and (b) clean syngas at 800 °C.

under 200 mW cm^{-2}. The cell demonstrated stability in this syngas blend, which is promising for future application of this composite anode.

3.3. Performance of SMM/GDC anode in H_2 with 10 ppm PH_3

An identical SMM/GDC cell was brought to 800 °C and 100 sccm wet H_2 and 150 sccm air were delivered to the anode and cathode respectively. Once the cell reached temperature, the slow anode reduction in 3% wet H_2 ensued until the open circuit voltage was observed. This voltage was found to be 1.046 V in wet H_2 upon full reduction. A constant current load of 0.25 A cm^{-2} was then applied to the cell. With the load, the corresponding voltage was measured as 0.766 V. Fig. 5 shows the initial cell stability in wet H_2 for almost 20 h at this load level without 10 ppm PH_3. After the initial 20 h break-in period, 10 ppm PH_3 was introduced into the fuel stream without unloading the cell. The 10 ppm PH_3 introduction resulted in an initial 1–2 mV drop in the cell potential. However, the cell quickly re-stabilized and remained at that potential for approximately 40 h. During that time, the ohmic resistance remained constant at 0.47 Ω cm^2, but the polarization resistance increased from 0.55 Ω cm^2 to 0.70 Ω cm^2, as quantified by the loaded EIS measurement that can been seen in Fig. 8.

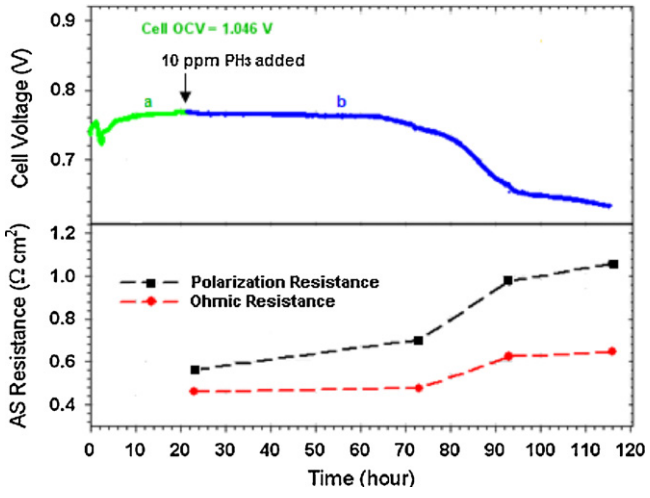

Fig. 5. Cell voltage and resistance vs. time for the electrolyte-supported SOFC with a SMM/GDC anode tested at 800 °C and at constant current density (0.25 A cm^{-2}) in (a) H_2 + 3% H_2O fuel and (b) H_2 + 3% H_2O with the addition of 10 ppm PH_3.

The values of the ohmic resistance and polarization resistance can be determined through visual inspection of a Nyquist plot. Much research has been done in correlating the geometry of these curves to the individual electrical and electrochemical processes that occur during SOFC operation [34–43]. Using the fundamental theory from these previous works, the ohmic resistance was determined by the intersection of the first arc with the real impedance axis. For thick electrolyte membranes, such as those used in this work, the majority of the ohmic resistance is aligned with the electrolyte membrane, which accounts for the movement of ions across the electrolyte. The magnitude of the polarization resistance was determined by measuring the distance between the first and second intersections with the real axis. This resistance may be attributed to both the high and low frequency processes, such as charge transfer and mass diffusion, respectively. Eq. (1) shows the total resistance of the circuit:

$$\Delta R_{\text{total}} = \Delta R_{\text{act}} + \Delta R_{\text{conc}} + \Delta R_{\Omega} \quad (1)$$

where ΔR_{act} is the activation polarization, ΔR_{conc} is the concentration polarization, and ΔR_{Ω} is the ohmic resistance. This fundamental theory was applied to the results to formulate initial conclusions about the performance of the cell over time.

After the initial 40 h of stability in 10 ppm PH_3, the cell potential decreases at a rate of about 2.8 mV h^{-1} over the course of the next 30 h. The series resistance increased to 0.16 Ω cm^2 and the polarization resistance continued to rise as well over this span. However, after 70 h in 10 ppm PH_3, the rate of cell degradation decreased to about 1 mV h^{-1} and the series resistance remained nearly constant while the polarization resistance increased about another 10%. The cell never re-stabilized beyond this time and continued to degrade at a similar rate. By the time the test was concluded, a 47% decrease in maximum power density was observed, as displayed in Fig. 6. Because the cell failed to re-stabilize over a significant range of time, the test was concluded.

While degradation to this SMM/GDC anode was shown in these tests, it shows much higher resistance to phosphine poisoning compared to the standard Ni/YSZ anode on an electrolyte-supported cell. Of course, we differentiate between anode-supported and electrolyte-supported designs, since the rate of anode degradation as a result of poisoning is dependent upon anode thickness. The electrolyte-supported platform was used in this study in order to accelerate degradation of the anode (due to minimal anode thickness) for rapid evaluation purposes. In Fig. 7, the voltage versus time comparison can be seen which indicates much stronger tolerance to PH_3 for the SMM/GDC anode. Within 30 h, the Ni/YSZ cell voltage drops to 0 V (~3.1 h^{-1} %) using the same testing

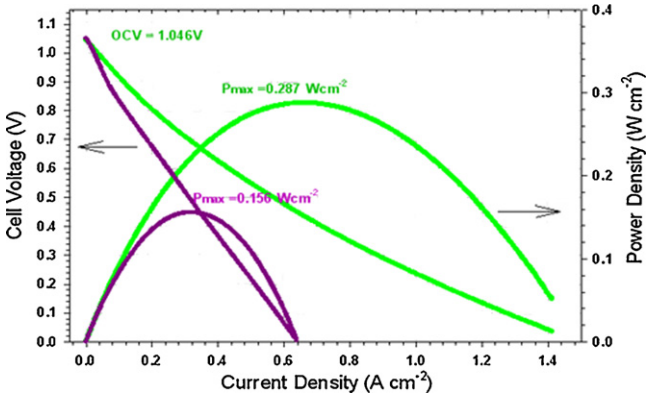

Fig. 6. *J–V–P* performance of SOFC with SMM/GDC anode in wet H_2 before PH_3 introduction and after 120 h of operation of 10 ppm PH_3.

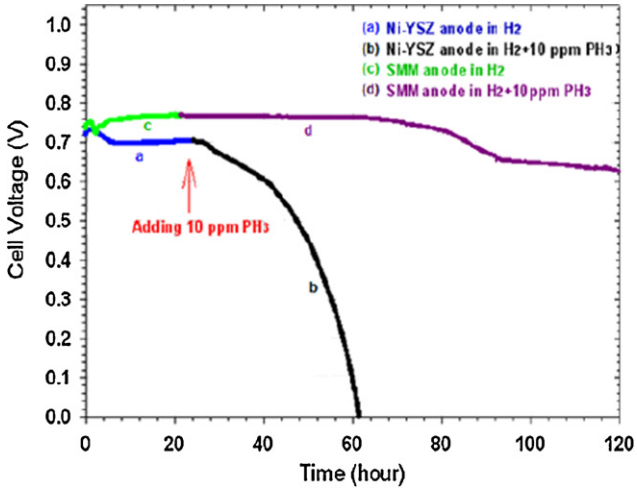

Fig. 7. Comparison of the performance at constant current density (0.25 A cm^{-2}) in wet H_2 and with addition of 10 ppm PH_3 between Ni-YSZ anode cell and SMM/GDC anode cell.

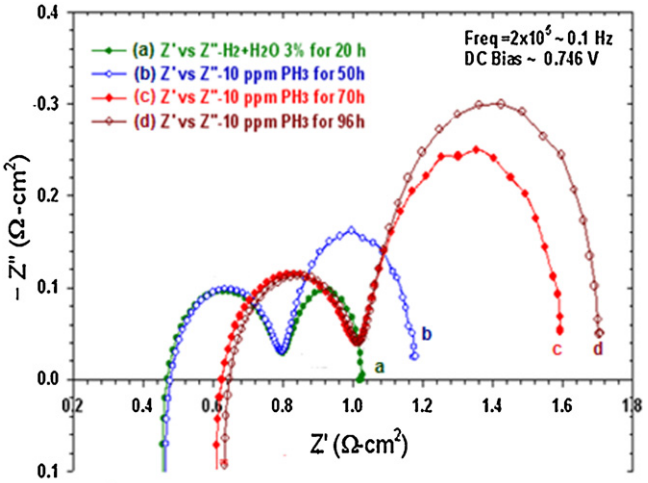

Fig. 8. EIS curves at 0.746 V bias before and after introducing 10 ppm PH_3 impurity into the H_2 fuel stream.

protocol and conditions. Extrapolation of the performance curve for the SMM/GDC anode would result in complete cell failure after approximately 750 h. The complete cell failure in this context indicates the point where the cell potential will reach a zero value.

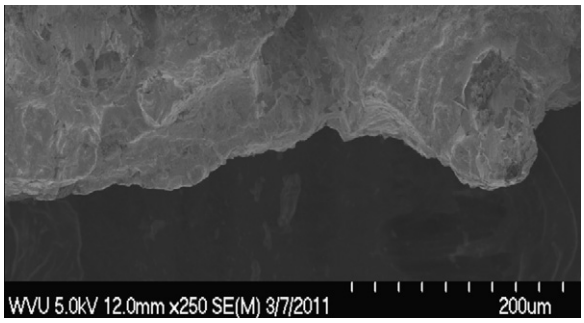

Fig. 10. Pt contact paste after exposure to 10 ppm PH_3. The Pt layer densified throughout the course of this test.

Fig. 8 shows the detailed progression of the Nyquist plots through the duration of the testing. After 50 h, no change in the ohmic resistance and the high frequency arc was observed. The only change during this time was an increase to the second arc. This increase in the second arc did not however affect the cell performance during this time.

Fig. 9 shows the microstructures of the bulk anode after testing in (A) wet, pure-H_2 and (B) 10 ppm PH_3 containing fuel. The images suggest small changes in the bulk anode microstructure throughout the duration of the testing. However, this microstructure is a far contrast from what is typically seen for poisoning of the Ni/YSZ anode, where the formation of phosphide and/or phosphate phases throughout the bulk of the anode results in vast microcracking, anode densification, and microstructural failure [44,45]. Therefore, the effect of microstructural change may not be the sole culprit for the performance degradation for the SMM/GDC composite anode. It was identified after post-mortem investigation that the microstructure of the Pt contact was vastly altered. Fig. 10 shows that the Pt contact material densified extensively and delamination was shown along the contact area between the anode and the lead wires. Both densification and delamination of these leads may contribute significantly to the restriction of fuel diffusion to the anode surface and current collection.

During the next 20 h, a 34% increase in the ohmic resistance and another increase in the second arc were observed. From this point to the conclusion of the test, increases to the polarization and series resistance were minimal. Fig. 11 indicates that the reasoning for the increase in series resistance may be due to slight delamination at the electrode/electrolyte interface, which would suggest that ion flow is being hindered. By the end of the test, the magnitude of the resistance from the first arc remains about the same, meaning that low frequency processes and increases to the ohmic resistance are ultimately responsible for the decrease in performance of the cell.

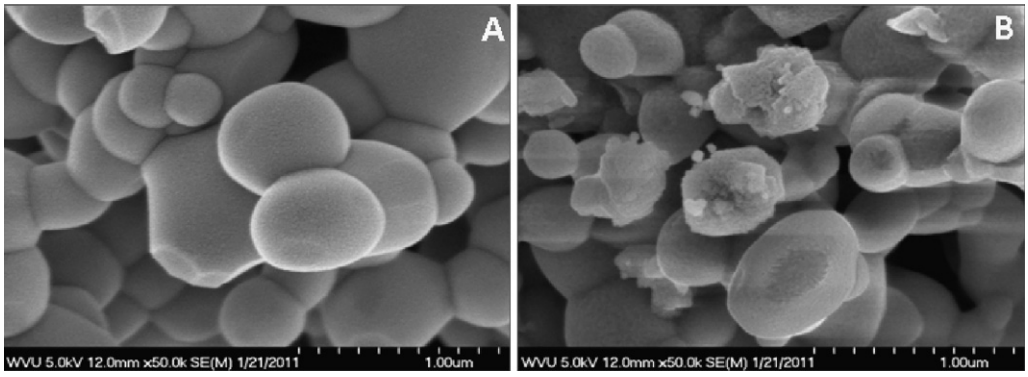

Fig. 9. SEM micrographs of the SMM/GDC anode after testing in (A) wet H_2 and (B) wet H_2 with 10 ppm PH_3. There appears to be no significant change to the microstructure of the bulk of the anode.

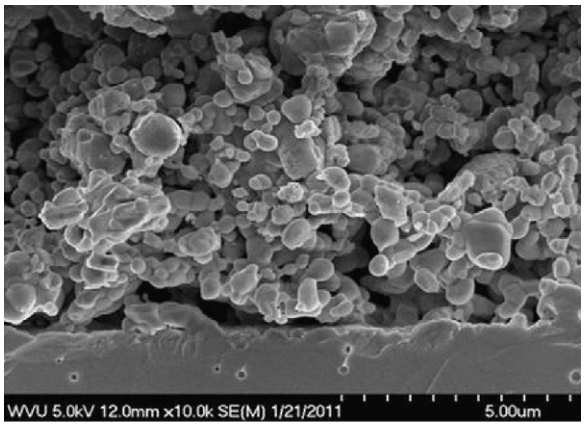

Fig. 11. SEM micrograph of the active anode/electrolyte interface after PH_3 poisoning test.

3.4. XPS/EDS analysis

The XPS spectrum along the anode/electrolyte interface from a cross-sectioned sample was completed to identify the formation of secondary phases, such as phosphide or phosphate compositions. One possibility would be for phosphorus to exist at the interface as either a phosphide or phosphate. Xu et al. [44] showed distinct peaks for P 2s and P 2p at 192 eV and 134 eV, respectively, where the 134 eV peak from their work corresponded to possible phosphate presence in the form of either P_2O_5 or PO_4^{3-}. Their XPS analysis also indicated potential nickel-phosphide phase formation from their Ni $2p_{3/2}$ peaks. These results were obtained using similar testing conditions to the work performed in this study; the only difference being that Xu et al. completed the testing in syngas with PH_3, which will be a focal point of future work for this SMM anode.

The XPS results from this fuel cell test show that no P 2s peak was detected near the active interface. Fig. 12 shows the overall spectra near the active interface with distinct peaks for each of the key anode components. Fig. 13 shows an enhanced view of the range where the P 2s peak would be expected. This lack of a peak is evidence to suggest that the phosphorus is not residing in the active interface. The P 2p peak however is more difficult to classify. Fig. 14 is the magnified XPS spectra corresponding to the P 2p peak. A fairly well-defined peak is present in the range of 132–134 eV, which could suggest that phosphate compounds were

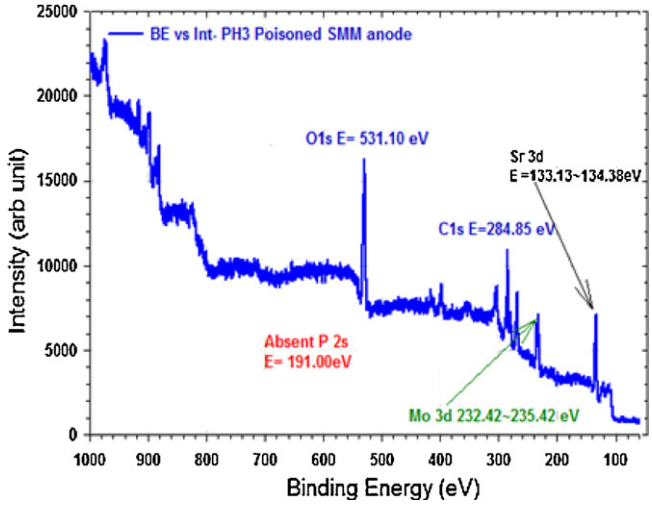

Fig. 12. XPS spectra of the anode/electrolyte interface following exposure to 10 ppm PH_3.

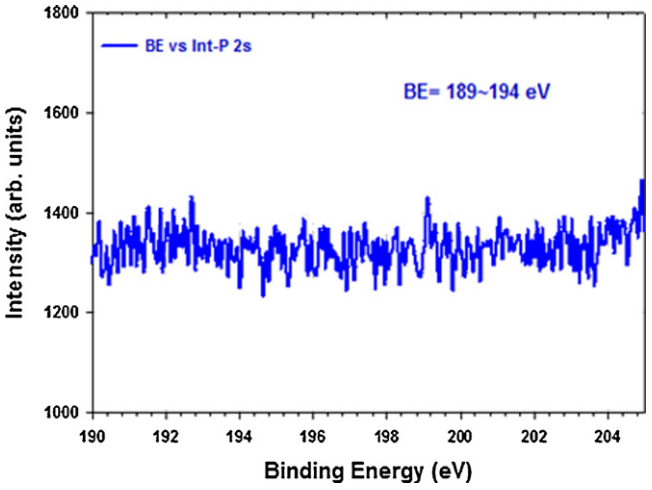

Fig. 13. An enhanced view of the XPS spectra with no change in signal at 192 eV where the P 2 s peak would be expected.

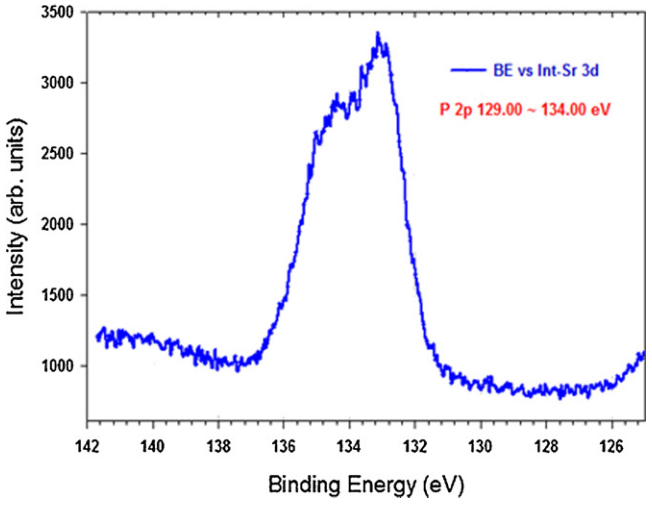

Fig. 14. An enhanced view of the XPS signal in the 134 eV range corresponding to the Sr 3d signal. This signal also corresponds to the P 2p peak and thus is not adequate for elemental qualification.

present in our sample. The problem is that this peak coincides with the Sr 3d peak, making it difficult to identify this peak using XPS alone. To help rectify this diagnostic problem, an EDS analysis was conducted in a similar location to distinguish between the two elements. The spectral plot in Fig. 15 shows a very distinct Sr peak

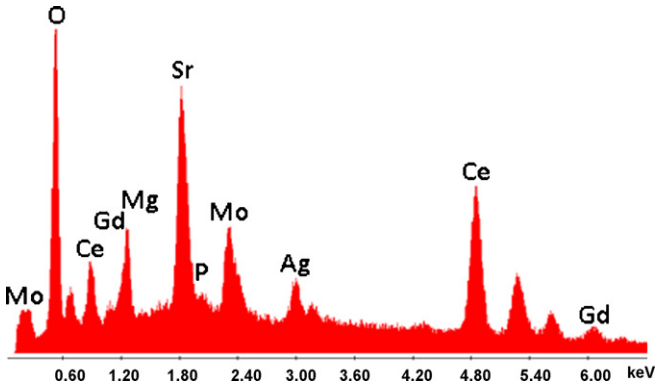

Fig. 15. EDS scan of the anode/electrolyte interface. The scan has a well defined Sr peak and a very weak signal for P.

and a very weak signal for P. This along with the lack of a P 2s peak cannot rule out that phosphorus is responsible for the degradation, but these results indicate a low P presence in the active region, thus diminishing the potential for microstructural alteration at the anode/electrolyte as the sole degradation mechanism.

4. Conclusions

A SMM/GDC composite SOFC anode composition was fabricated and tested on an electrolyte-supported platform in humidified H_2 and coal syngas fuels. The GDC was found to greatly improve the performance of the cell and is primarily aiding in the anode's ionic conduction. The cell exhibited stability in wet hydrogen and the performance of the cell remained the same after the first 50 h in 10 ppm PH_3. After this however, the cell potential decreased and never fully re-stabilized. The rate of degradation of this composite anode was much lower than that of the standard Ni/YSZ anode, which signifies the value of this work. The XPS and EDS spectra of the anode/electrolyte interface did not distinctly confirm the presence of secondary phase formation. This result is in far contrast to that seen for typical Ni/YSZ anodes exposed to phosphine. We are initially attributing power degradation to slight anode de-lamination and mass diffusion limitations from contact paste densification. However, due to the initial stability of this cell in 10 ppm PH_3, future work will focus on modifications to the anode architecture and current collection in order to optimize performance and demonstrate increased contact stability. In addition, fundamental mechanistic studies are required to better understand the lower rate of electrochemical and microstructural degradation for this ceramic composite compared to the typical Ni/YSZ cermet anode. Better understanding of the interaction of the phosphine with this all-ceramic anode will provide valuable information in the pursuit of developing a high-performance anode that may function on coal-syngas fuel with reasonable levels of H_2S and PH_3 contaminants.

Acknowledgements

This work is conducted under US DOE EPSCoR Program. It is jointly sponsored by US DOE Office of Basic Energy Sciences, NETL (National Energy Technology Laboratory), WV State EPSCoR Office, and West Virginia University under grant number DE-FG02-06ER46299. Ms. Adrienne MacLeod and Dr. Hui Zhang are thanked for assistance with the SEM, EDS, and XPS characterization. ANH refractories are also thanked for assistance with iso-static pressing of samples.

References

[1] S.C. Singhal, K. Kendall, High Temperature Solid Oxide Fuel Cells, Elsevier Ltd., 2003.
[2] S.M. Haile, Acta Mater. 51 (2003) 5981–6000.
[3] M. Li, A.D. Rao, J. Brouwer, G.S. Samuelsen, J. Power Sources 195 (2010) 5707–5718.
[4] R.S. Gemmen, J. Trembly, J. Power Sources 161 (2006) 1084.
[5] E.H. Pacheco, M.D. Mann, P.N. Hutton, D. Singh, K.E. Martin, J. Hydrogen Energy 30 (2005) 1221–1233.
[6] H. Miao, W.G. Wang, T.S. Li, T. Chen, S.S. Sun, C. Xu, J. Power Sources 195 (2010) 2230–2235.
[7] G. Krishnan, Proc. 9th Annual Solid State Energy Conversion Alliance Workshop, Pittsburgh, PA, USA, August 5–7, 2008.
[8] J.P. Trembly, R.S. Gemmen, D.J. Bayless, Proc. 5th International Fuel Cell Science, Engineering and Technology Conference, New York, NY, 2007.
[9] M.J. Zhi, X.Q. Chen, H. Finklea, I. Celik, N.Q. Wu, J. Power Sources 183 (2008) 485–490.
[10] O.A. Marina, C.A. Coyle, E.C. Thomsen, D.J. Edwards, G.W. Coffey, L.R. Pederson, Solid State Ionics 181 (2010) 430–440.
[11] A. Lussier, S. Sofie, J. Dvorak, Y.U. Idzerda, J. Hydrogen Energy 33 (2008) 3945–3951.
[12] E.L. Hardegree, P. Ho, J.M. White, Surf. Sci. 165 (1986) 488–506.
[13] M. Blaszczyszyn, R. Blaszczyszyn, R. Meclewski, Surf. Sci. 131 (1983) 433–447.
[14] L. Zhang, S.P. Jiang, H.Q. He, X. Chen, J. Ma, X.C. Song, J. Hydrogen Energy 35 (2010) 1259–1268.
[15] C.M. Grgicak, R.G. Green, J.B. Giorgi, J. Power Sources 179 (2008) 317–328.
[16] J.P. Trembly, A.I. Marquez, T.R. Ohrni, D.J. Bayless, J. Power Sources 158 (2006) 263–273.
[17] M. Flytzani-Stephanopoulos, M. Sakbodin, Z. Wang, Science 312 (2006) 1508–1510.
[18] H. Devianto, J. Power Sources 159 (2006) 1147–1152.
[19] R.J. Gorte, H. Kim, J.M. Vohs, J. Power Sources 106 (2002) 10–15.
[20] Z.F. Zhou, J. Power Sources 133 (2004) 181–187.
[21] H. He, R.J. Gorte, J.M. Vohs, Electrochem. Solid State Lett. 8 (2005) 279–280.
[22] M.R. Pillai, I. Kim, D.M. Bierschenk, S.A. Barnett, J. Power Sources 185 (2008) 1086–1093.
[23] H. Kurokawa, L. Yang, C.P. Jacobson, L.C. De Jonghe, S.J. Visco, J. Power Sources 164 (2007) 510–518.
[24] S. Zha, P. Tsang, Z. Cheng, M. Liu, J. Solid State Chem. 178 (2005) 1844–1850.
[25] C. Yates, J. Winnick, J. Electrochem. Soc. 146 (1999) 2841–2844.
[26] Z. Cheng, S. Zha, L. Aguilar, M. Liu, Solid State Ionics 176 (2005) 1921–1928.
[27] J.B. Goodenough, Y.H. Huang, J. Power Sources 173 (2007) 1–10.
[28] Y.H. Huang, R.I. Dass, J.C. Denyszyn, J.B. Goodenough, J. Electrochem. Soc. 153 (2006) A1266.
[29] Y.H. Huang, R.I. Dass, Z.L. Xing, J.B. Goodenough, Science 312 (2006) 254.
[30] D. Marrero-Lopez, J. Pena-Martınez, J.C. Ruiz-Morales, D. Perez-Coll, M.A.G. Aranda, P. Nunez, Mater. Res. Bull. 43 (2008) 2441–2450.
[31] S. Vasala, M. Lehtimaki, S.C. Haw, J.M. Chen, R.S. Liu, H. Yamauchi, M. Karppinen, Solid State Ionics 181 (2010) 754–759.
[32] D. Marrero-López, J. Peña-Martínez, J.C. Ruiz-Morales, M. Gabás, P. Núñez, M.A.G. Aranda, J.R. Ramos-Barrado, Solid State Ionics 180 (2010) 1672–1682.
[33] D.H. Prasad, H.R. Kim, J.S. Park, J.W. Son, B.K. Kim, H.W. Lee, J.H. Lee, J. Alloy. Compd. 495 (2010) 238–241.
[34] Q.A. Huang, R. Hui, B. Wang, J. Zhang, Electrochim. Acta 52 (2007) 8144–8164.
[35] S.B. Adler, Solid State Ionics 111 (1998) 125–134.
[36] S.B. Adler, B.T. Henderson, M.A. Wilson, D.M. Taylor, R.E. Richards, Solid State Ionics 135 (2000) 35–42.
[37] W.G. Bessler, Solid State Ionics 176 (2005) 997–1011.
[38] F. Zhao, A.V. Virkar, J. Power Sources 141 (2005) 79–95.
[39] M. Mogensen, K.V. Jensen, M.J. Jørgensen, S. Primdahl, Solid State Ionics 150 (2002) 123–129.
[40] P. Singhal, K. Kawagoe, C.N. Christian, W.G. Kulr, Anal. Chem. 69 (1997) 1662.
[41] J.R. Wilson, D.T. Schwartz, S.B. Adler, Electrochim. Acta 51 (2006) 1389.
[42] J.R. Macdonald, D.R. Franceschetti, J. Chem. Phys. 68 (1978) 1614.
[43] M.J. Jørgensen, S. Primdahl, M. Mogensen, Electrochim. Acta 44 (1999) 4195–4201.
[44] C. Xu, J.W. Zondlo, H. Finklea, O. Demircan, M. Gong, X. Liu, J. Power Sources 193 (2009) 739–746.
[45] C. Xu, J.W. Zondlo, M. Gong, X. Liu, J. Power Sources 196 (2011) 116–125.